Glutamate “flick” enables proton tunneling during fast redox biocatalysis

Stephen B Carr,[1,2*] Wangzhe Li,[1‡] Kin-Long Wong,[1,2‡] Rhiannon M Evans,[1] Sophie E.T. Kendall-Price,[1] Kylie A Vincent[1*] and Philip A Ash[3,4*]

[1]University of Oxford, Department of Chemistry, Inorganic Chemistry Laboratory, South Parks Road, Oxford, OX1 3QR, U.K., [2]Research Complex at Harwell, Rutherford Appleton Laboratory, Harwell Campus, Didcot, OX11 0FA, U.K. [3]School of Chemistry, University of Leicester, University Road, Leicester, LE1 7RH, U.K. [4]Leicester Institute for Structural and Chemical Biology, University of Leicester, Leicester, UK

‡ These authors contributed equally.

Abstract

Redox enzymes capable of carrying out multi-electron reactions serve as blueprints for the rational design of bio-inspired catalysts for future green technologies.[1–4] During catalysis, enzymes transition through multiple ‘active’ intermediate states. Movement of both electrons and substrate to/from the active site is precisely controlled to achieve the equivalent of high Faradaic efficiencies, with minimal electrons wasted in detrimental side reactions. High turnover frequencies in metalloenzymes such as the nickel-iron (NiFe) hydrogenases require mechanisms for highly-choreographed movement of two quantum particles, protons and electrons.[5] According to Marcus theory, structural rigidity is key to a low reorganisation energy barrier for rapid, outer-sphere electron transfer.[6] However, this is at odds with the requirement for a degree of conformational flexibility to enable rapid proton tunnelling between residues separated by distances greater than ~2.7 Å.[7,8] Here we exploit the specific redox poising possible with electrochemical control of protein crystals[9,10] and characterise, structurally and spectroscopically, [NiFe]-hydrogenase in each of the key states of the catalytic cycle as well as its CO-bound and oxidised states. These structures confirm extraordinarily fixed metal coordination at the active site, conducive to fast multi-electron catalysis, and reveal a subtle carboxylate ‘flick’ that provides molecular detail of how glutamate acts as a proton shuttle.

Main

Global cycles of hydrogen, nitrogen, and carbon are underpinned by reduction and oxidation (redox) processes. Catalysis of these redox transformations represent some of the greatest challenges to renewable fuels, sustainable agriculture, carbon dioxide capture, and decarbonisation of chemical manufacturing. In nature, hydrogen, nitrogen, and carbon cycles are controlled by ancient metalloenzymes which exploit readily-bioavailable metals for finely-tuned redox catalysis. NiFe-hydrogenases have attracted attention for their ability to catalyse rapid H_2 oxidation or production at an active site built from earth-abundant metals (Fig. 1 and Extended data Figure 1).[11] Four strictly conserved cysteine residues anchor the nickel iron active site, two terminal to nickel, and two which bridge the metals. The Fe atom remains formally divalent Fe(II) and is further coordinated by one CO and two CN^- ligands, which serve as sensitive infrared spectroscopic reporters on the state of the active site. Reactivity is nickel-centred and exploits formal oxidation states of Ni(III/II/I). Electrons are shuttled via a chain of iron sulfur clusters which intimately affect the catalytic properties at the active site.[12–16]Present understanding of the catalytic cycle (Extended data Fig. 1) comes from spectroscopic, computational, and biochemical studies[17] with only limited structural evidence for the interplay between the active site and the wider protein matrix due to the difficulty in trapping specific intermediates in a multi-state redox enzyme. Recently, we have demonstrated electrochemical

control over protein crystals, with in situ infrared microspectroscopy,[9,10] to provide a roadmap for generation of hydrogenase crystals in specific, catalytically-relevant, redox states (Fig. S1). Here we apply this approach to electrochemically poise crystals of two [NiFe]-hydrogenases from *E. coli*, Hyd-1, and Hyd-2, in well-defined and spectroscopically-verified redox states, allowing generation of atomic-resolution structures of each catalytically-relevant state (Extended data Fig. 2). Crucially, we report structural details of intermediates involved in the removal of protons from the [NiFe] active site during catalytic H_2 oxidation. These results resolve the knowledge-gap between existing reported structures (in which there are no amino acid residues within hydrogen-bonding distance of the active site)[18,19] and current kinetic studies[20,21] that suggest involvement of proton tunnelling (requiring a hydrogen-bonding connection of no more than 2.7 Å). Our results allow us to present a model for how a finely-tuned redox enzyme combines the active site rigidity required for rapid electron transfer with a state-specific conformational flick that enables proton transfer to keep pace with catalytic turnover.

Structures at the Ni_a-SI level reveal active-site associated water.

We first demonstrate redox-targeted x-ray diffraction for hydrogenase by solving structures of electrochemically poised Hyd-1 and Hyd-2 at the Ni_a-SI level, at resolutions of 1.45 and 1.37 Å, respectively. The structures both reveal a partially-ordered water molecule located 1.9 Å from active-site Ni (Fig. 1, Extended data Fig. 3). This offers the first direct evidence that the Ni_a-SI state is hydrated,[22] and suggests the possibility of a functionally-relevant water molecule in the active site region (see supplementary data for expanded discussion of other Ni_a-SI structures).

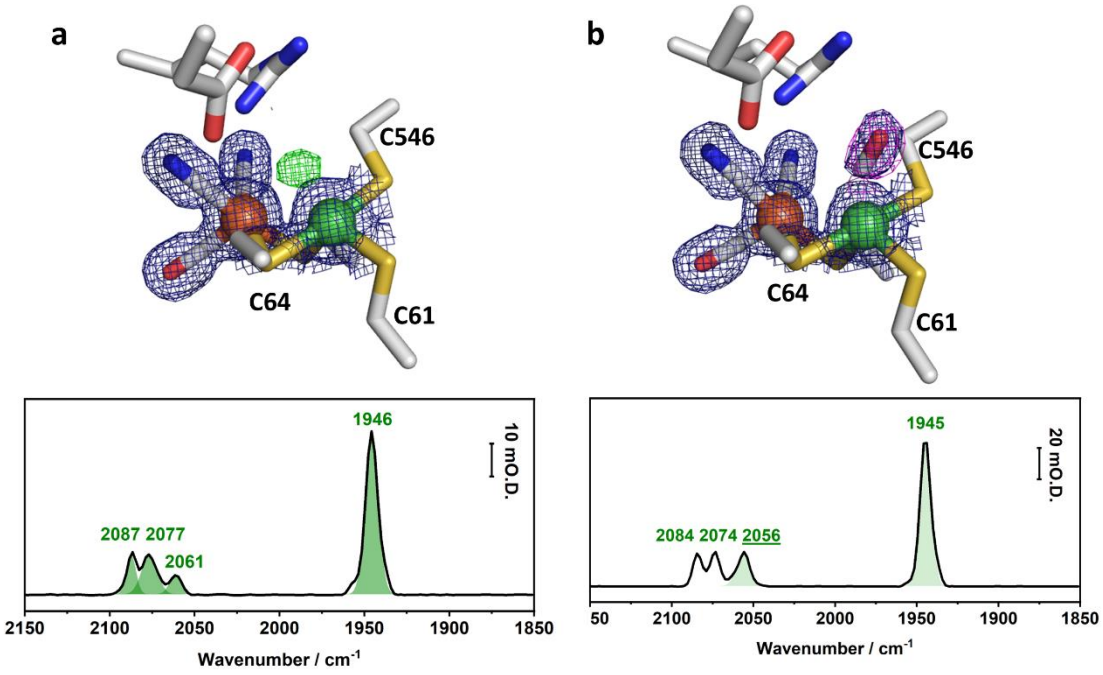

Fig. 1. (a) Crystal structure of Hyd-2 in the Ni_a-SI state shows the active site contains a Ni-coordinated water molecule (green mesh) and the associated IR spectrum shows a single ν(CO) centred at 1946 cm^{-1}, characteristic of Ni_a-SI. (b) Structure and IR-spectrum of Ni_a-SCO state of Hyd-2 shows the inhibitor coordinated to the Ni atom, producing a diagnostic peak at 2056 cm^{-1}.

Exogenous CO binds to an oxygen-tolerant hydrogenase

The identity of Ni_a-SI in Hyd-2 crystals was further confirmed by reaction with CO to generate the inhibited, Ni-SCO state. Hyd-2 crystals at the Ni_a-SI level show the expected spectroscopic changes consistent with binding of exogeneous CO. The structure shows clear electron density for a diatomic ligand bound to Ni (Fig. 1b), readily modelled as CO with a coordination distance of 1.8 Å and a Ni-C-O bond angle of 154°, similar to other CO-bound structures.[23–25] Although O_2-tolerant hydrogenases are generally thought to be relatively insensitive CO,[26] we also find clear spectroscopic and structural evidence for exogenous CO binding to Hyd-1 (Extended data Fig. 4).

Ni_a-C is structurally similar to Ni_a-R

Electrochemical reduction of Hyd-1 crystals at the Ni_a-SI level results in the Ni_a-R family of sub-states (Extended Data Fig. 1), all Ni(II) species which share a bridging hydride but are proposed to differ in the position of a proton close to the active site.[27] The electron density at the NiFe cofactor in our electrochemically-poised Ni_a-R crystal shows a significant peak in the Fo-Fc map (Fig. 2, green mesh) between the active site metals, the geometry of which is consistent with a bridging hydride. Furthermore, superposition of an ultra-high (0.89 Å) resolution structure of the Ni_a-R state in *Desulfovibrio vulgaris* Miyazaki F hydrogenase (pdb 4U9H) places the modelled hydride within the electron density peak of the structure reported herein (Extended Data Fig. 5).

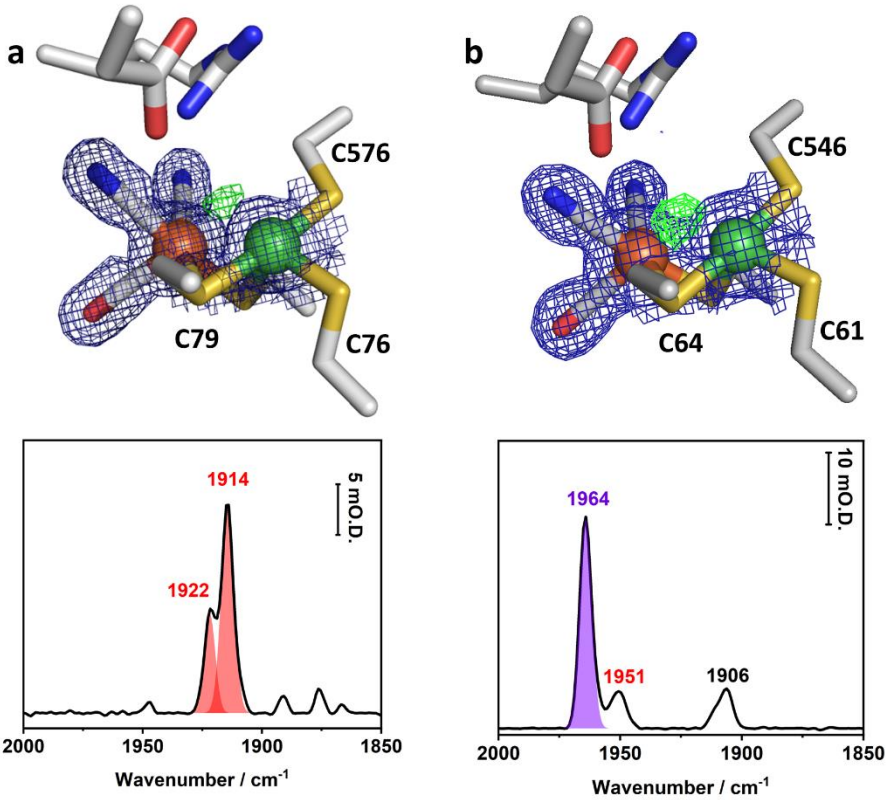

Fig. 2. (a) Crystal structure and IR spectrum of Hyd-1 in the Ni_a-R state. The crystals contain a mixture of Ni_a-R_{II} (1922 cm^{-1}) and Ni_a-R_{III} (1914 cm^{-1}) sub-states that differ in the position of the proton that migrates from the active site after hydrogen splitting (Extended Data Fig.1) (b) Crystal structure and IR spectrum of Hyd-2 poised at Ni_a-C level (1964 cm^{-1}). Both states show strong peaks in the Fo-Fc electron density maps (green mesh) at the same, bridging, position between the metal atoms that can be attributed to the bound hydride. Spectra showing ν(CO) and ν(CN) shown in fig. S4.

Proton-coupled removal of an electron from Ni_a-R produces Ni_a-C, formally at the Ni(III) level. Electrochemical poising of Hyd-2 crystals yielded ~95% Ni_a-C speciation, and the resulting crystal structure retains Fo-Fc electron density between the active-site metal atoms in the same position as that observed for Ni_a-R consistent with retention of the bridging hydride (Fig. 2, Table S3). Comparing the primary coordination sphere of the active site in the Ni_a-R and Ni_a-C states show the protein structure is unchanged (Table S4) even though the [NiFe] cluster has formally lost one electron altering the distribution of charge across the metals (Fig. 2b).

Localised structural flexibility in Ni_a-L assists H^+ transfer

To study the hydrogenase at the formal level of Ni(I) in the Ni_a-L family of substates, we first turn to Hyd-1 where Ni_a-L has been observed as a long-lived intermediate during turnover.[28] Electrochemical poising at a mild potential generated a mixture of states dominated by Ni_a-L species, and in particular the Ni_a-L_{II} state (>60 %, Fig. 3a), where L_I, L_{II}, and L_{III} are hypothesised to represent sequential proton movements away from the active site.[27] The structure of the primary coordination sphere of the active site is unchanged relative to Ni_a-C or Ni_a-R, (Table S4), but crucially lacks difference density between Ni and Fe, indicative of a vacant bridging position and loss of the bound hydride (Fig. 3a).

Of the conserved amino acid residues in the outer coordination sphere, only the side-chain of E28 moves on formation of Ni_a-L_{II} (Table S4). Rotation of E28, to a "swung in" position, places the carboxylate side chain within hydrogen-bonding distance of C576, shortening the oxygen-sulfur distance from 3.5 to 2.7 Å (Fig. 3b). This implies that one of the participating atoms must be protonated and provides the first direct structural evidence of how E28 enables proton transfer during catalysis.[29–32] Based on structural and steady-state kinetic data, E28 has long been implicated as the start point for several possible routes of proton egress from the active site,[33,34] with proton transfer assumed to occur via a Grotthuss-like hopping mechanism. However, large kinetic isotope effects (>40) have been demonstrated for a [NiFe]-hydrogenase from *P. furiosus* on sub-turnover timescales, which implies quantum tunnelling of protons [20,21] in turn requiring a hydrogen bonding pathway to provide the short donor-acceptor distance necessary for tunnelling. The state-specific glutamate "flick" (Fig. 3b) that brings E28 within hydrogen bonding distance of the active site, precisely when proton transfer is required, rationalises how E28 is essential for catalysis when all previously published structures have donor-acceptor distances too great (~3.5 Å) to allow proton tunnelling. Movement of E28 is also in agreement with molecular dynamics simulations that previously suggested conformational flexibility of the equivalent residue, E13, of *A. aeolicus* membrane-bound hydrogenase.[35] The characteristic timescales for sidechain rotations (nano to picoseconds)[36] are sufficiently short that a glutamate flick is compatible with catalytic turnover on the order of milli to-microseconds typically observed for [NiFe]-hydrogenase.[37] In the Ni_a-SI, Ni_a-C, and Ni_a-R structures, E28 is in the 'swung out' position forming a short (2.5 Å) hydrogen bond to highly conserved residue T18 in the small subunit (Extended Data Fig. 6). Such a short bond will raise the p*K*a of E28,[38] enhancing its ability to accept protons.

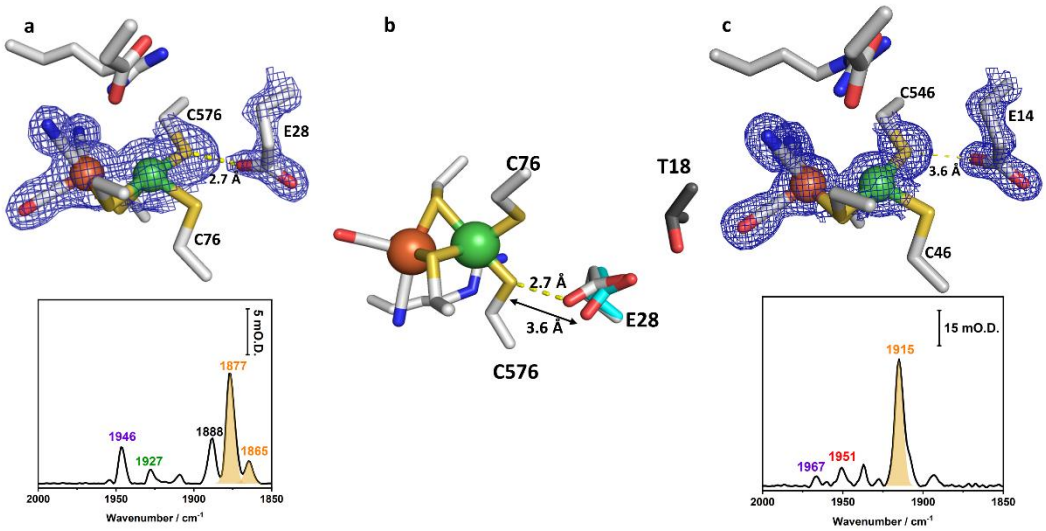

Fig. 3 (a) Hyd-1 crystals poised at −275 mV are highly enriched in the Ni_a-L_{II} state (1877 cm^{-1}, with minor species: Ni-L(iii) 1865 cm^{-1}), Ni-C (1946 cm^{-1}), Ni-SI (1927 cm^{-1}), and an unknown state (1888 cm^{-1}) present). Residue E28 twists towards the active site forming a hydrogen bond with C576, allowing proton egress from the metal centre. (b) Modest rotation of E28 towards C576 is sufficient to form a hydrogen bond to the active site in the 'swung in' position (white); the 'swung out' position of E28 in Ni-SI (cyan) is overlayed for comparison. (c) Structure and IR spectrum of Hyd-2 crystal poised at −600 mV followed by illumination with light at 365 nm (Extended Data Fig. 7) produces crystals containing the Ni_a-L_I state (1915 cm^{-1}) as the overwhelming majority species, here the side-chain of E14 (E28 in Hyd1) is too far away to interact with Ni-coordinating C546 (C576 in Hyd-1).

It is well established, for various hydrogenases, that photolysis of Ni_a-C is an alternative method to generate Ni_a-L states.[39,40] Illuminating cryogenically-cooled crystals of Hyd-2 poised at the Ni_a-C state with UV light produces crystals with IR spectra consistent with Ni_a-L_I (>98 %, Extended Data Fig 7), in which the proton is proposed to reside on an active-site cysteine.[41–43] Structurally, Ni_a-L_I appears identical to Ni_a-C, with E14 (E28 in Hyd-1) remaining in the 'swung out' position, but with complete loss of the bridging hydride ligand in Ni_a-L_I. (Fig. 3c, Extended Data 8). In the Ni_a-R structure (Fig. 2), derived from a mixture of the Ni_a-R_{II} and Ni_a-R_{III} states, E28 is also in the 'swung out' position, while this does not preclude a role for E28 in proton transfer at the Ni_a-R level it suggests each proton produced during H_2 oxidation may have a different exit pathway.

Fine potential control uncouples structural changes at the active site and proximal cluster.

Poising Hyd-1 crystals at progressively more oxidising potentials (Fig. 4) isolates the Ni-B state with each structure showing clear electron density for a hydroxide bridging the Ni and Fe atoms. [19] Unlike air-oxidation of Hyd-1 there is no indication of oxygenation of any of the active site cysteine residues, indicative of Ni-A.[44] At +100 mV the proximal cluster remains in the closed conformation[45] with the mobile Fe atom (Fe7) coordinated by the side-chains of C19 and C20 (Extended Data Fig 9). Analysis of difference maps suggest the closed conformation is present in >90% of molecules in the crystal lattice. The closed conformation of the proximal cluster is typically associated with the reduced (+3) state,[30,46] however, since the applied potential lies between the mid-point potentials of the oxidised (+30 mV) and superoxidised (+230 mV) states of this cluster,[14] and oxidation typically results in only a

slight contraction of Fe-S bond-lengths,[47] it is likely the cluster is, in fact, in the oxidised (+4) state. This is the first time this has been isolated for oxygen-tolerant hydrogenases, where oxidised enzyme typically displays proximal clusters as a mixture of oxidised and superoxidised conformations[30,48] or wholly in the superoxidised (+5) state.[30,49]

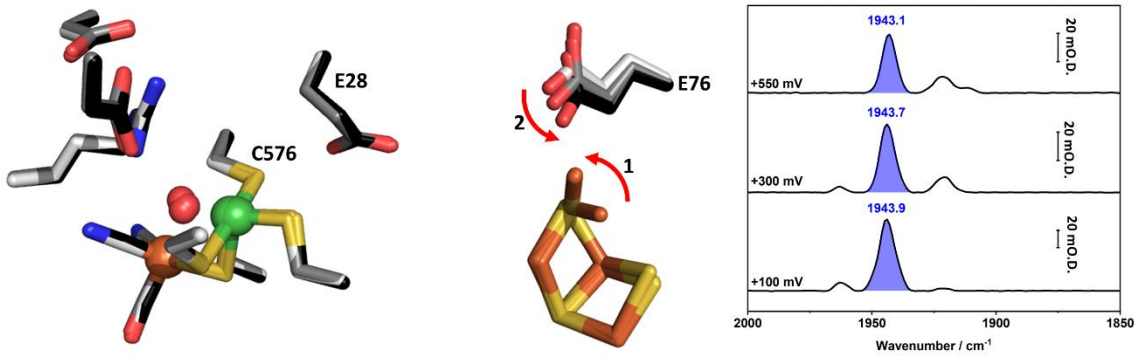

Fig. 4: (a) Superposed structures of oxidised active site and proximal FeS cluster of Hyd-1 show conformational changes that occur as the enzyme responds to oxidative inactivation, +100 mV state shown in white, +300 mV state shown in grey and +550 mV state shown in black. (b) Stacked spectra of νCO region measured under the same oxidative potentials shows the majority species to be Ni-B (1943cm^{-1}). Full spectra including CN region is shown in Extended Data Fig. 9a.

Stepping the applied potential to +300 mV triggers the majority (>90%) of the proximal cluster to switch to the open, superoxidised (+5) conformation with the mobile Fe now additionally coordinated by the main-chain amide group of C20 (Extended Data Fig. 7c). A further step towards a more positive potential (+550 mV) causes the side-chain of Glu76 to swing towards the mobile Fe atom, coordinating the metal and further stabilising the superoxidised conformation. Previous analysis of oxidised Hyd-1 structures[30] suggested mobility of E76 allowed the carboxylate group to accept a proton from the backbone amide of C20, facilitating coordination to Fe7. However, our structures do not support this since the +300 mV state shows the mobile Fe is already coordinated by the mainchain amide of C20, implying deprotonation, before any movement of E76 that could aid proton abstraction has occurred. This suggests the role of E76 is to electrostatically stabilise the most oxidised state of the cluster. The structure of Hyd-2 poised at +200 mV (Extended Data Fig. 10) captures the pure Ni-B state of this enzyme, with a hydroxide bridging the Ni and Fe atoms and no trace of oxidation of the coordinating Cys ligands or elsewhere in the protein.

Conclusions

We have independently isolated, verified, and structurally characterised each long-lived redox intermediate of the [NiFe]-hydrogenase catalytic cycle. Minimal structural changes are observed in the primary coordination sphere between catalytically-active redox states of the [NiFe]-hydrogenase active site, even with a 1 electron reduction from Ni_a-C to Ni_a-R. This is entirely consistent with a low reorganisation energy for electron tunnelling as required by Marcus theory. Structural rigidity extends to the highly-conserved amino acid residues surrounding the [NiFe]-active site with the notable exception of a single glutamate residue, E28 (in Hyd-1, E14 in Hyd-2). We provide direct evidence for how H^+ transfer during catalysis is facilitated by a subtle flick of this glutamate sidechain, specific to the Ni_a-L_{II} state, to bring it within the 2.7 Å distance required for proton tunnelling. This reconciles the

seemingly incompatible observations of proton tunnelling and a large donor-acceptor distance in [NiFe]-hydrogenases, demonstrating a new paradigm for highly-optimised proton-coupled electron transfer.

Methods

Electrochemical poising apparatus

A general workflow for electrochemical poising of protein crystals prior to x-ray diffraction is detailed in Extended Data Fig. 2. The two-component 'crystal vial' system used for electrochemical poising of protein crystals comprises a large electrochemical cell for bulk electrochemistry and a separate, smaller vial for introducing mediator to the protein crystals. The two parts are connected via a peristaltic pump to circulate the crystallisation buffer containing electrochemical mediators (Tables S5 and S6). The separation is necessary to 1) protect the crystals from the shear forces generated by rapid stirring of the solution in the electrochemical cell, necessary to efficiently poise the mediator solution, and 2) to allow for gentle introduction of the mediator to the crystals. These measures were essential for maintaining the diffraction quality of the crystals. Constant pumping of mediator-containing crystallisation buffer ensured the crystals were continually exposed to freshly-poised mediator at a defined potential. Electrochemical potential were applied with an AutoLab 128 N potentiostat (Metrohm) controlled by NOVA software (v 1.10) Electrochemical potentials (E) were measured with a saturated calomel reference electrode (SCE) and potentials quoted in the text adjusted to mV *vs* the standard hydrogen electrode (SHE) using the conversion *E* (mV *vs* SHE) = *E* (mV *vs* SCE) +241 mV at 25 °C.[50]

Purification and crystallisation of Hyd-1 and Hyd-2

Proteins were expressed, purified, and crystallised as described previously,[44,51] with all "as-isolated" crystals predominantly in the Ni-B state, as assessed by IR-spectroscopy.[10]

Electrochemical poising of Hyd-1 crystals

A solution (5 mL) containing appropriate redox mediator(s) (Table S6), each at 1 mM concentration, was prepared in N_2 saturated crystallisation buffer (100 mM Bis-Tris, pH 6, 200 mM Li_2SO_4, 150 mM NaCl, 22% w/v PEG 3350, 15% v/v glycerol) and transferred into the electrochemical cell in a N_2-filled glovebox (Belle Technologies or Glove Box Technologies, O2 <3 ppm). The mediator solution was initially poised at −600 mV *vs.* SHE until the mixture reached equilibrium, as judged by the measured current approaching zero mA, to ensure full reduction of the mediators (Extended Data Fig. 2). Then a 10 µL aliquot of the poised mediator cocktail was added to each well of a crystallisation plate containing Hyd-1 crystals, to initiate reductive activation of the protein. Multiple crystals were then transferred from crystallisation plate to the crystal vial by gentle pipetting. The crystal vial was then topped up with 300 µL poised mediator solution and the crystals allowed to settle for approximately 5 mins. Poised mediator solution was then flowed across the crystals for at least 8 hours to ensure complete electrochemical activation of Hyd-1. It should be noted that unlike Hyd-2, exposure of crystals of Hyd-1 to pure hydrogen gas was insufficient to reductively activate the protein (Fig. S2). The potential was then switched to the target potential, to enrich the crystals in the desired redox state. The target potential was applied until equilibrium, judged by the measured current approaching 0 mA, was achieved (Extended Data Fig. 2). The poised crystals were transferred with 20 µL poised mediator solution to an empty well on a crystallisation plate, some were flash-cooled in liquid N_2 under anaerobic conditions for x-ray diffraction measurements while others were transferred to a transmission cell for IR spectroscopy to confirm the speciation within the crystal.

Electrochemical poising of Hyd-2 crystals

Hyd-2 crystals were electrochemically poised at the desired potentials in Hyd-2 crystallisation buffer (100 mM Bis-Tris, pH 6, 200 mM $MgCl_2$, 22% w/v PEG 3350, 15% v/v glycerol). Hyd-2 crystals were activated either by electrochemical reduction as described for Hyd-1 or by exposure to pure H_2. For H_2 activation, a 10 µL aliquot of the crystallisation buffer was added to each well of the crystallisation plates containing Hyd-2 crystals. The crystals were then transferred into a 600 µL microcentrifuge tube with 50 µL crystallisation buffer. The open microcentrifuge tube was then placed into a sealed vial, which was flushed with 100% H_2 with a flow of 10 mL/min for at least one hour. The spectrum of the Hyd-2 crystal after H_2 activation is shown in Fig. S3 and shows a complete absence of any inactivated-active site states (Ni-B or Ni-A, 1957 cm^{-1}).

Like Hyd-1, mediator solutions (5 mL) were poised at −600 mV *vs.* SHE for one hour to fully reduce the mediator followed by a switch to the target potential for at least one hour or until equilibrium was achieved. At this point the H_2-activated Hyd-2 crystals were loaded into the crystal vial, followed by topping up with the poised solution to 300 µL. The crystals were further poised at the chosen potential for at least one hour before harvesting for XRD and FTIR measurements as described for Hyd-1 above.

Single crystal infrared spectroscopy measurements

For each batch of poised crystals FTIR spectra were measured to confirm the speciation at the active site. Since spectra could not be directly measured for the samples used for diffraction experiments, spectra were recorded for multiple crystals from each poising experiment to ensure there has been a uniform response to the applied potential throughout each batch of poised crystals. The poised crystals were anaerobically pipetted, in 20 µL of poised mediator solution to a transmission IR cell, and sandwiched between two CaF_2 windows separated by a 50 µm spacer. Extended Data Fig. 2 shows an image of a poised crystal recorded through a 15× objective lens. The IR spectra were recorded using a Vertex 70 FTIR spectrometer (Bruker) equipped with a Hyperion 2000 microscope and a mercury cadmium telluride (MCT) detector. IR spectra were recorded from a sample area defined by motorised slits in the IR beam path. Background spectra were recorded from a sample of the poised mediator solution at a position adjacent to the single crystal sample. All spectra were recorded over 50 scans at resolutions of 2 or 4 cm^{-1}using OPUS 8.2.28 software. Origin 2023 software was used for subsequent baseline correction, using an interpolated spline function, and fitting Gaussian functions to the observed peaks.

Single crystal infrared spectroscopy measurement on Hyd-2 crystals at low temperature

Hyd-2 crystals were electrochemically poised at the Ni_a-C state and then pipetted anaerobically with 12 µL poised Eu-BAPTA solution to a transmission IR cell (PIKE Technologies). IR spectra were recorded at room temperature to confirm speciation. The transmission IR cell containing the crystals was then placed in liquid N_2 for several minutes prior to recording a cryogenic "dark" reference spectrum under ambient laboratory illumination or a "light" spectrum after illumination for 10 s with a 365 nm LED (Thorlabs). The "light" and "dark" crystal IR spectra were recorded at 2 cm^{-1} resolution for 50 scans.

Light triggering of frozen Hyd-2 crystals prior to X-ray diffraction data collection

Hyd-2 crystals that were poised at Ni_a-C state were flash-cooled in liquid N_2. Crystals were mounted onto the goniometer of beamline I24 (Diamond Light Source) and held in a stream of N_2 gas at 100 K before illumination with an LED with a centre wavelength of 365 nm (Thorlabs) for 10 seconds. Diffraction data were collected after the illumination using x-rays of wavelength of 0.62 Å and an Eiger2 XE 16M detector.

X-ray structure determination

After poising, crystals were flash-cooled in liquid N_2 prior to data collection. Diffraction data were collected as helical scans and low x-ray doses (to minimise radiation damage (Fig. S5, Tables S7-S10) at beamlines I03 or I24 (Diamond Light Source, UK) using x-rays of wavelength 0.77 Å and an Eiger2 XE 16M detector. Data reduction was performed using DIALS[52] and AIMLESS[53] within the Xia2 pipeline[54]. Using REFMAC5[55], initial phase estimates were generated by all atom refinement of wild-type hydrogenase (pdb 6FPO) against data collected from poised crystals. The resulting maps were inspected in COOT[56] followed by iterative rounds of manual rebuilding (COOT) and refinement (REFMAC5[55] or PHENIX[57]) until no further improvements were possible. The quality of the resulting models was assessed using Molprobity[58]. Relative proportions of different states of the proximal cluster were estimated by deleting atoms Fe from the cluster, calculating omit maps and comparing peak heights in the resultant Fo-Fc map.

Acknowledgements

We thank Diamond Light Source for access to beamlines I03 and I04 (MX23459 and MX31353) where all crystallographic data were collected. We also thank Diamond Light source for access to the MIRIAM beamline B22 (SM21651 and SM33329) that contributed to the results presented here. The work of K.A.V. and S.B.C. has been supported by the Biotechnology and Biological Sciences Research Council (BBSRC grants BB/R018413/1 and BB/X002624/1) and P.A.A. is supported by BB/X002292/1. K.A.V. is grateful for financial support from a European Research Council grant (ERC-2018-CoG BiocatSusChem 819580). S.E.T.K.-P. received support from an EPSRC Studentship Grant EP/N509711/1.

Author Contributions

S.B.C, R.M.E, P.A.A and K.A.V conceived and designed experiments. S.B.C and K.L.W purified and crystallised hydrogenase proteins. W.L. developed electrochemical poising methodology, conducted crystal poising, and collected the majority of IR spectra prior to structure determination. K.L.W poised crystals, measured IR spectra and solved x-ray structures of Ni_a-C, Ni_a-L_I and Ni_a-L_{II} states. S.B.C solved all other crystal structures. R.M.E and S.E.T.K-P collected and analysed all IR spectra used to generate speciation curves used to guide poising experiments. S.B.C, P.A.A and K.A.V wrote the manuscript with editorial contributions from all authors.

Competing Interests

The authors declare no competing interests.

References

1. Ji, H. *et al.* Hydrogenase as the basis for green hydrogen production and utilization. *Journal of Energy Chemistry* vol. 85 348–362 Preprint at https://doi.org/10.1016/j.jechem.2023.06.018 (2023).

2. Hardt, S. *et al.* Reversible H2 oxidation and evolution by hydrogenase embedded in a redox polymer film. *Nat Catal* **4**, 251–258 (2021).

3. Trncik, C., Detemple, F. & Einsle, O. Iron-only Fe-nitrogenase underscores common catalytic principles in biological nitrogen fixation. *Nat Catal* **6**, 415–424 (2023).

4. Brazzolotto, D. *et al.* Nickel-centred proton reduction catalysis in a model of [NiFe] hydrogenase. *Nat Chem* **8**, 1054–1060 (2016).

5. Reece, S. Y. & Nocera, D. G. Proton-coupled electron transfer in biology: Results from synergistic studies in natural and model systems. *Annual Review of Biochemistry* vol. 78 673–699 Preprint at https://doi.org/10.1146/annurev.biochem.78.080207.092132 (2009).

6. Marcus, R. A. On the theory of oxidation-reduction reactions involving electron transfer. I. *J Chem Phys* **24**, 966–978 (1956).

7. Zaragoza, J. P. T. *et al.* Temporal and spatial resolution of distal protein motions that activate hydrogen tunneling in soybean lipoxygenase. *Proc Natl Acad Sci U S A* **120**, (2023).

8. Hammes-Schiffer, S. Hydrogen tunneling and protein motion in enzyme reactions. *Acc Chem Res* **39**, 93–100 (2006).

9. Ash, P. A. *et al.* Generating single metalloprotein crystals in well-defined redox states: Electrochemical control combined with infrared imaging of a NiFe hydrogenase crystal. *Chemical Communications* **53**, 5858–5861 (2017).

10. Ash, P. A. *et al.* The crystalline state as a dynamic system: IR microspectroscopy under electrochemical control for a [NiFe] hydrogenase. *Chem Sci* **12**, 12959–12970 (2021).

11. Vignais, P. M. & Billoud, B. Occurrence, classification, and biological function of hydrogenases: An overview. *Chemical Reviews* vol. 107 4206–4272 Preprint at https://doi.org/10.1021/cr050196r (2007).

12. Lukey, M. J. *et al.* Oxygen-tolerant [NiFe]-hydrogenases: The individual and collective importance of supernumerary cysteines at the proximal Fe-S cluster. *J Am Chem Soc* **133**, 16881–16892 (2011).

13. Evans, R. M. *et al.* Principles of sustained enzymatic hydrogen oxidation in the presence of oxygen -the crucial influence of high potential Fe-S clusters in the electron relay of [NiFe]-hydrogenases. *J Am Chem Soc* **135**, 2694–2707 (2013).

14. Roessler, M. M., Evans, R. M., Davies, R. A., Harmer, J. & Armstrong, F. A. EPR spectroscopic studies of the Fe-S clusters in the O2- tolerant [NiFe]-hydrogenase Hyd-1 from Escherichia coli and characterization of the unique [4Fe-3S] cluster by HYSCORE. *J Am Chem Soc* **134**, 15581–15594 (2012).

15. Goris, T. *et al.* A unique iron-sulfur cluster is crucial for oxygen tolerance of a [NiFe]-hydrogenase. *Nat Chem Biol* **7**, 310–318 (2011).

16. Pandelia, M.-E. *et al.* Characterization of a unique [FeS] cluster in the electron transfer chain of the oxygen tolerant [NiFe] hydrogenase from Aquifex aeolicus. *PNAS* **108**, 6097–6102 (2011).

17. Lubitz, W., Ogata, H., Rüdiger, O. & Reijerse, E. Hydrogenases. *Chemical Reviews* vol. 114 4081–4148 Preprint at https://doi.org/10.1021/cr4005814 (2014).

18. Ogata, H., Nishikawa, K. & Lubitz, W. Hydrogens detected by subatomic resolution protein crystallography in a [NiFe] hydrogenase. *Nature* **520**, 571–574 (2015).

19. Hiromoto, T. *et al.* New insights into the oxidation process from neutron and X-ray crystal structures of an O2-sensitive [NiFe]-hydrogenase. *Chem Sci* (2023) doi:10.1039/d3sc02156d.

20. Greene, B. L., Vansuch, G. E., Wu, C. H., Adams, M. W. W. & Dyer, R. B. Glutamate Gated Proton-Coupled Electron Transfer Activity of a [NiFe]-Hydrogenase. *J Am Chem Soc* **138**, 13013–13021 (2016).

21. Greene, B. L., Vansuch, G. E., Chica, B. C., Adams, M. W. W. & Dyer, R. B. Applications of Photogating and Time Resolved Spectroscopy to Mechanistic Studies of Hydrogenases. *Acc Chem Res* **50**, 2718–2726 (2017).

22. Caserta, G. *et al.* Hydroxy-bridged resting states of a [NiFe]-hydrogenase unraveled by cryogenic vibrational spectroscopy and DFT computations. *Chem Sci* **12**, 2189–2197 (2021).

23. Ilina, Y. *et al.* X-ray Crystallography and Vibrational Spectroscopy Reveal the Key Determinants of Biocatalytic Dihydrogen Cycling by [NiFe] Hydrogenases. *Angewandte Chemie - International Edition* **58**, 18710–18714 (2019).

24. Imanishi, T. *et al.* Structural and spectroscopic characterization of CO inhibition of [NiFe]-hydrogenase from Citrobacter sp. S-77. *Acta Crystallogr F Struct Biol Commun* **78**, 66–74 (2022).

25. Ogata, H. *et al.* Structural studies of the carbon monoxide complex of [NiFe]hydrogenase from Desulfovibrio vulgaris Miyazaki F: Suggestion for the initial activation site for dihydrogen. *J Am Chem Soc* **124**, 11628–11635 (2002).

26. Pandelia, M. E., Infossi, P., Giudici-Orticoni, M. T. & Lubitz, W. The oxygen-tolerant hydrogenase i from Aquifex aeolicus weakly interacts with carbon monoxide: An electrochemical and time-resolved FTIR study. *Biochemistry* **49**, 8873–8881 (2010).

27. Ash, P. A., Hidalgo, R. & Vincent, K. A. Proton Transfer in the Catalytic Cycle of [NiFe] Hydrogenases: Insight from Vibrational Spectroscopy. *ACS Catal* **7**, 2471–2485 (2017).

28. Hidalgo, R., Ash, P. A., Healy, A. J. & Vincent, K. A. Infrared spectroscopy during electrocatalytic turnover reveals the Ni-L active site state during H2 oxidation by a NiFe hydrogenase. *Angewandte Chemie - International Edition* **54**, 7110–7113 (2015).

29. Sumner, I. & Voth, G. A. Proton transport pathways in [NiFe]-hydrogenase. *Journal of Physical Chemistry B* **116**, 2917–2926 (2012).

30. Volbeda, A. *et al.* X-ray crystallographic and computational studies of the O 2-tolerant [NiFe]-hydrogenase 1 from Escherichia coli. *Proceedings of the National Academy of Sciences USA* **109**, 5305–5310 (2012).

31. Galván, I. F., Volbeda, A., Fontecilla-Camps, J. C. & Field, M. J. A QM/MM study of proton transport pathways in a [NiFe] hydrogenase. *Proteins: Structure, Function and Genetics* **73**, 195–203 (2008).

32. Teixeira, V. H., Soares, C. M. & Baptista, A. M. Proton pathways in a [NiFe]-hydrogenase: A theoretical study. *Proteins: Structure, Function and Genetics* **70**, 1010–1022 (2008).

33. Dementin, S. *et al.* A Glutamate is the Essential Proton Transfer Gate during the Catalytic Cycle of the [NiFe] Hydrogenase. *Journal of Biological Chemistry* **279**, 10508–10513 (2004).

34. Evans, R. M. *et al.* Mechanistic Exploitation of a Self-Repairing, Blocked Proton Transfer Pathway in an O2-Tolerant [NiFe]-Hydrogenase. *J Am Chem Soc* **140**, 10208–10220 (2018).

35. Oteri, F., Baaden, M., Lojou, E. & Sacquin-Mora, S. Multiscale simulations give insight into the hydrogen in and out pathways of [NiFe]-hydrogenases from aquifex aeolicus and desulfovibrio fructosovorans. *Journal of Physical Chemistry B* **118**, 13800–13811 (2014).

36. Nam, K. & Wolf-Watz, M. Protein dynamics: The future is bright and complicated! *Structural Dynamics* **10**, (2023).

37. Aldinio-Colbachini, A. *et al.* Transport limited adsorption experiments give a new lower estimate of the turnover frequency of Escherichia coli hydrogenase 1. *BBA Advances* **3**, (2023).

38. Herschlag, D. & Pinney, M. M. Hydrogen Bonds: Simple after All? *Biochemistry* vol. 57 3338–3352 Preprint at https://doi.org/10.1021/acs.biochem.8b00217 (2018).

39. Fichtner, C., Van Gastel, M. & Lubitz, W. Wavelength dependence of the photo-induced conversion of the Ni-C to the Ni-L redox state in the [NiFe] hydrogenase of Desulfovibrio vulgaris Miyazaki F. *Physical Chemistry Chemical Physics* **5**, 5507–5513 (2003).

40. Pandelia, M. E., Ogata, H. & Lubitz, W. Intermediates in the catalytic cycle of [NiFe] hydrogenase: Functional spectroscopy of the active site. *ChemPhysChem* vol. 11 1127–1140 Preprint at https://doi.org/10.1002/cphc.200900950 (2010).

41. Dong, G. & Ryde, U. Protonation states of intermediates in the reaction mechanism of [NiFe] hydrogenase studied by computational methods. *Journal of Biological Inorganic Chemistry* **21**, 383–394 (2016).

42. Kampa, M., Pandelia, M. E., Lubitz, W., Van Gastel, M. & Neese, F. A metal-metal bond in the light-induced state of [nife] hydrogenases with relevance to hydrogen evolution. *J Am Chem Soc* **135**, 3915–3925 (2013).

43. Siebert, E. *et al.* Resonance raman spectroscopy as a tool to monitor the active site of hydrogenases. *Angewandte Chemie - International Edition* **52**, 5162–5165 (2013).

44. Evans, R. M. *et al.* Mechanism of hydrogen activation by [NiFe] hydrogenases. *Nat Chem Biol* **12**, 46–50 (2016).

45. Grubel, K. & Holland, P. L. New iron-sulfur clusters help hydrogenases tolerate oxygen. *Angewandte Chemie - International Edition* **51**, 3308–3310 (2012).

46. Aragão, D. *et al.* Reduced hybrid cluster proteins (HCP) from Desulfovibrio desulfuricans ATCC 27774 and Desulfovibrio vulgaris (Hildenborough): X-ray structures at high resolution using synchrotron radiation. *Journal of Biological Inorganic Chemistry* **8**, 540–548 (2003).

47. Ohno, H. *et al.* Crystallographic characterization of the highpotential iron-sulfur protein in the oxidized state at 0.8 Å resolution. *PLoS One* **12**, (2017).

48. Shomura, Y., Yoon, K. S., Nishihara, H. & Higuchi, Y. Structural basis for a [4Fe-3S] cluster in the oxygen-tolerant membrane-bound [NiFe]-hydrogenase. *Nature* **479**, 253–256 (2011).

49. Frielingsdorf, S. *et al.* Reversible [4Fe-3S] cluster morphing in an O 2 -tolerant [NiFe] hydrogenase. *Nat Chem Biol* **10**, 378–385 (2014).

50. Faulkner L.R. & Bard A.J. *Electrochemical Methods*. (Wiley, New York, 2001).

51. Beaton, S. E. *et al.* The structure of hydrogenase-2 from Escherichia coli: Implications for H2-driven proton pumping. *Biochemical Journal* **475**, 1353–1370 (2018).

52. Waterman, D. G. *et al. The DIALS Framework for Integration Software*. www.biostruct-x.org.

53. Evans, P. R. & Murshudov, G. N. How good are my data and what is the resolution? *Acta Crystallogr D Biol Crystallogr* **69**, 1204–1214 (2013).

54. Winter, G. Xia2: An expert system for macromolecular crystallography data reduction. *J Appl Crystallogr* **43**, 186–190 (2010).

55. Murshudov, G. N. *et al.* REFMAC5 for the refinement of macromolecular crystal structures. *Acta Crystallogr D Biol Crystallogr* **67**, 355–367 (2011).

56. Emsley, P., Lohkamp, B., Scott, W. G. & Cowtan, K. Features and development of Coot. *Acta Crystallogr D Biol Crystallogr* **66**, 486–501 (2010).

57. Afonine, P. V. *et al.* Joint X-ray and neutron refinement with phenix.refine. *Acta Crystallogr D Biol Crystallogr* **66**, 1153–1163 (2010).

58. Richardson, J. S. *et al.* Model validation: Local diagnosis, correction and when to quit. *Acta Crystallogr D Struct Biol* **74**, 132–142 (2018).